

¹ **The Impact of Large-Scale Orography on Northern Hemisphere Winter**

² **Synoptic Temperature Variability**

³ Nicholas J. Lutsko*

⁴ *Department of Earth, Atmospheric, and Planetary Sciences, Massachusetts Institute of*
⁵ *Technology, Cambridge, Massachusetts*

⁶ Jane W. Baldwin

⁷ *Princeton Environmental Institute, Princeton University, Princeton, New Jersey*

⁸ Timothy W. Cronin

⁹ *Department of Earth, Atmospheric, and Planetary Sciences, Massachusetts Institute of*
¹⁰ *Technology, Cambridge, Massachusetts*

¹¹ *Corresponding author address: Nicholas Lutsko, Department of Earth, Atmospheric, and Planetary Sciences, Massachusetts Institute of Technology, Cambridge, Massachusetts
¹³ E-mail: lutsko@mit.edu

ABSTRACT

14 The impact of large-scale orography on wintertime temperature variability
15 on daily and synoptic time-scales (days to weeks) in the Northern Hemisphere
16 is investigated. Using a combination of theory, idealized modeling work and
17 simulations with a comprehensive climate model, it is shown that large-scale
18 orography reduces upstream temperature gradients, in turn reducing upstream
19 temperature variability, and enhances downstream temperature gradients,
20 enhancing downstream temperature variability. Hence the presence of the
21 Rockies on the western edge of the North American continent increases
22 temperature gradients over North America and, consequently, increases North
23 American temperature variability. By contrast, the presence of the Tibetan
24 Plateau and the Himalayas on the eastern edge of the Eurasian continent
25 damps temperature variability over most of Eurasia. However, Tibet and the
26 Himalayas also interfere with the downstream development of storms in the
27 North Pacific storm track, and thus damp temperature variability over North
28 America, by approximately as much as the Rockies enhance it.

29

30 Large-scale orography is also shown to impact the skewness of down-
31 stream temperature distributions, as temperatures to the north of the enhanced
32 temperature gradients are more positively skewed while temperatures to the
33 south are more negatively skewed. This effect is most clearly seen in the
34 northwest Pacific, off the east coast of Japan.

³⁵ **1. Introduction**

³⁶ Temperature variability is one of the most important features of the climate for human society
³⁷ and natural ecosystems, affecting, among many other things, agricultural and economic produc-
³⁸ tion (Lazo et al. (2011); Wheeler and von Braun (2013); Shi et al. (2015); Jahn (2015); Bathi-
³⁹ any et al. (2018)) and the rhythmns of ecological seasons (Jackson et al. (2009); Bowers et al.
⁴⁰ (2016)). Changes in temperature variability may be among the most impactful aspects of future
⁴¹ climate change, which has motivated much recent work on the mechanisms controlling temper-
⁴² ature variability in present and future climates, with two primary foci: (1) the question of how
⁴³ Arctic amplification will influence mid-latitude temperature variability; and (2) the question of
⁴⁴ what controls the zonal-mean variance and higher-order moments of the temperature distribution
⁴⁵ (e.g., Schneider et al. (2015); Garfinkel and Harnik (2017); Linz et al. (2018)). With respect to
⁴⁶ Arctic amplification, it is now clear that mid-latitude zonal-mean temperature variance will be
⁴⁷ reduced (Screen (2014); Schneider et al. (2015); Hoskins and Woollings (2015)), though the ef-
⁴⁸ fect of Arctic amplification on higher moments of mid-latitude temperature distributions is still
⁴⁹ uncertain (e.g., Cohen et al. (2014); Barnes and Polvani (2015)).

⁵⁰ Little work, however, has been done to understand what controls regional (zonally-asymmetric)
⁵¹ patterns of temperature variability, despite their societal relevance. For instance, changes in heat-
⁵² waves with global warming can be well predicted by superposing a mean shift on present-day
⁵³ daily temperature variability, so that understanding the pattern of temperature variance is key for
⁵⁴ forecasting spatial variations in heat-wave changes with warming (Rahmstorf and Coumou (2011);
⁵⁵ Lau and Nath (2012); Lau and Nath (2014); Huybers et al. (2014); McKinnon et al. (2016)).

⁵⁶ An example of a regional difference in temperature variability can be seen in panels a and b of
⁵⁷ Figure 1. Whether using daily data (panel a) or filtering to synoptic time-scales (days to weeks,

58 panel b), North America experiences substantially more near-surface temperature variability than
59 Eurasia during boreal winter (December–January–February, DJF, see section 2 for description of
60 observational dataset). This is also shown by Figure 1e, which plots a longitudinal profile of DJF
61 synoptic temperature variance at 50°N: temperature variance at this latitude is roughly twice as
62 large over North America as over Eurasia. Investigating the contribution of large-scale Northern
63 Hemisphere orography (Asian orography, which includes the Himalayas, the Tibetan Plateau and
64 the Mongolian Plateau, and the Rockies) to the enhancement of temperature variability over North
65 America compared to Eurasia is the primary goal of the present study.

66 Our analysis is based on the dominant control of winter synoptic temperature variability by hor-
67 izontal advection, which implies in turn that mean horizontal temperature gradients, particularly
68 meridional gradients, are the primary control on synoptic temperature variability (Schneider et al.
69 (2015); Holmes et al. (2016); see section 3a below). It can be seen in panels c and d of Figure
70 1 that both zonal and meridional temperature gradients are larger over North America than over
71 Eurasia during winter, suggesting that whatever causes these enhanced gradients is also responsi-
72 ble for the enhanced variability over North America. More generally, the importance of meridional
73 temperature gradients for synoptic temperature variability suggests a close link between the North-
74 ern Hemisphere winter stationary wave pattern and the regional distribution of winter temperature
75 variability.

76 Waves forced by large-scale orography are a key component of the winter stationary wave pattern
77 in the Northern Hemisphere (Held et al. 2002). Below, we show that orography increases down-
78 stream temperature gradients and decreases upstream temperature gradients, with corresponding
79 impacts on temperature variability. We demonstrate this mechanism in simulations with two ide-
80 alized atmospheric general circulation models (GCMs), one dry and one moist, which allows us
81 to investigate how the shape of the orography influences its impact on temperature variability and

82 how moist processes impact the dynamics (section 3). We then present simulations with a com-
83 prehensive climate model in which the major Northern Hemisphere mountain ranges are flattened,
84 to quantify the impact these have on winter temperature variability (section 4). A complicating
85 factor is orography's effect on downstream development: the presence of large-scale orography
86 can weaken downstream eddies by interfering with the recycling of energy from upstream, leading
87 to reduced temperature variability far from the orography.

88 By enhancing and reducing mean temperature gradients, orography also impacts the skewness
89 of temperature distributions, which we explore in section 5. We end with conclusions in section 6.

90 **2. Data and Methods**

91 *a. Observational Data*

92 Observational data are taken from the Modern-Era Retrospective Analysis for Research and
93 Applications (MERRA) dataset (Rienecker et al. 2011). The MERRA grid has 1.25° resolution
94 in latitude and longitude, and we have taken daily-averaged data from December, January and
95 February for the years 1979 to 2012.

96 *b. Dry GCM*

97 The dry GCM is the GFDL spectral dynamical core, which solves the primitive equations for
98 a dry ideal gas on the sphere, and is forced by Newtonian relaxation to a prescribed zonally-
99 symmetric equilibrium temperature field and damped by Rayleigh friction near the surface. The
100 parameter settings are the standard Held-Suarez parameters with forcing symmetric about the
101 equator (Held and Suarez 1994). This set-up produces an equinoctial climate similar to that of the
102 real atmosphere, though the north-south temperature gradient is somewhat larger than observed
103 and temperature is uniform in the stratosphere.

104 As in Lutsko and Held (2016), the model is perturbed by adding a Gaussian mountain, with the
105 form

$$h(\phi, \lambda) = H \exp \left\{ - \left[\frac{(\phi - \phi_0)^2}{\alpha^2} + \frac{(\lambda - \lambda_0)^2}{\beta^2} \right] \right\}, \quad (1)$$

106 where H is the maximum height of the mountain in meters; λ and ϕ are longitude and latitude,
107 respectively; λ_0 and ϕ_0 are the co-ordinates of the center of the mountain; and α and β are half-
108 widths, both set to 15° in the main suite of simulations. λ_0 and ϕ_0 were set to 90°E and 45°N ,
109 respectively, in all simulations.

110 H was varied from 333m, which is in the “linear” regime, with air mostly flowing up and over
111 the mountain, to 4km, which is in the “non-linear” regime, with air mostly deflected around that
112 orography (Lutsko and Held 2016). In every simulation, the model was run at T85 resolution
113 with 30 evenly spaced sigma levels and data were sampled once per day. We present results from
114 simulations lasting 5000 days, with data taken from the final 4000 days.

115 *c. Moist GCM*

116 The moist GCM is the gray-radiation model first described by Frierson et al. (2006), though
117 we have used the parameter settings of O’Gorman and Schneider (2008), and also included their
118 parameterization of short-wave absorption by the atmosphere. The model uses the GFDL spectral
119 dynamical core, and includes the simplified Betts-Miller (SBM) convection scheme of Frierson
120 (2007). The moist GCM is coupled to a slab ocean of depth 1m, with no representation of ocean
121 dynamics or of sea ice. A mixed-layer depth of 1m was used so that the model would spin up
122 quickly, while leaving the resulting mean climate similar as for larger mixed layer depths. We
123 show results using a convective relaxation time-scale τ_{SBM} of 2 hours and a reference relative

¹²⁴ humidity $RH_{SBM} = 0.7$. The boundary layer scheme is the one used by O’Gorman and Schneider
¹²⁵ (2008).

¹²⁶ The same Gaussian orography is added to the model as in the primitive equation model, except
¹²⁷ we only consider a case with $H = 4000\text{m}$ and circular orography, centered further north at 60°N .
¹²⁸ The reason for moving the orography poleward is that the maximum temperature variability is
¹²⁹ further north in this set-up (see Figure 5), so a more northward mountain produces clearer changes
¹³⁰ in variance. As discussed by Wills and Schneider (2018), this implementation produces an “aqua-
¹³¹ mountain”, and the surface fluxes over the orography are not necessarily realistic. However, any
¹³² bias in surface fluxes is of secondary importance for our investigation.

¹³³ The moist GCM was integrated at T85 truncation with 30 unevenly-spaced vertical levels, start-
¹³⁴ ing from a state with uniform SSTs. The simulations lasted for 4500 days with data stored four
¹³⁵ times per day, and we have taken averages over the final 4000 days.

¹³⁶ *d. Comprehensive climate model*

¹³⁷ The comprehensive climate model is GFDL CM2.5-FLOR (Vecchi et al. 2014). FLOR stands for
¹³⁸ Forecast-oriented Low Ocean Resolution, and the model is based on the GFDL CM2.5 model. It
¹³⁹ is run with an atmospheric resolution of approximately 50km and an oceanic resolution of approx-
¹⁴⁰ imately 1° . By running with a relatively high resolution atmosphere, FLOR is able to accurately
¹⁴¹ capture many subseasonal forms of variability, such as hurricanes and monsoon depressions, and
¹⁴² can resolve sharp topographic features, such as the peaks of the Himalayas (compare panels a and
¹⁴³ b of Figure 2).

¹⁴⁴ Three simulations were performed with FLOR: (1) a control simulation with present-day to-
¹⁴⁵ pography, (2) a simulation with the Rockies flattened to 300m (the “no-Rockies” simulation, i.e.,
¹⁴⁶ all surface heights greater than 300m are reduced to 300m) and (3) a simulation with the Asian

¹⁴⁷ orography (the Tibetan Plateau, the Himalayas and the Mongolian Plateau) flattened to 300m (the
¹⁴⁸ “no-Tibet” simulation). The regions of flattened topography can be seen in Figure 2 and we note
¹⁴⁹ that the gravity wave drag and boundary layer roughness were fixed to their control values where
¹⁵⁰ the topography was flattened.

¹⁵¹ All simulations were conducted with pre-industrial radiative forcings, matching the best guess
¹⁵² for the year 1860, and with static vegetation. Data were collected once per day for 50 years,
¹⁵³ following 100 years of spin-up from an initial state of rest, and SSTs were relaxed to a repeating
¹⁵⁴ climatology with a relaxation time-scale of five days. This set-up was originally designed to allow
¹⁵⁵ tropical cyclones to interact with the ocean surface (Vecchi et al. 2014); for our purposes, the
¹⁵⁶ model is essentially an atmosphere-only climate model run over fixed SSTs. Our configuration
¹⁵⁷ attempts to isolate the direct effects of the orographic forcing on temperature variability, though
¹⁵⁸ not the indirect effects orography has on variability through its impact on SSTs.

¹⁵⁹ *e. Filtering to synoptic time-scales*

¹⁶⁰ The data were filtered to synoptic time-scales using a fourth-order Butterworth filter, with cut-
¹⁶¹ off frequencies of $1/3$ days $^{-1}$ and $1/15$ days $^{-1}$. The filter was implemented using the Python
¹⁶² package `scipy.signal`, with the filter co-efficients obtained using `scipy.signal.butter` and
¹⁶³ the filtering done with `scipy.signal.lfilter`. We have verified that our results are robust to
¹⁶⁴ the choice of filtering time-scales, within reason. For all datasets, DJF variance and skewness were
¹⁶⁵ calculated individually for each year (e.g., December 1979 to February 1980) and then averaged
¹⁶⁶ over all years to find the climatological variance and skewness.

167 **3. Impact of Orography on Temperature Variance in Idealized Models**

168 *a. Background theory*

169 Assuming that synoptic potential temperature variations are primarily generated by horizontal
170 advection, and that this advection is local in time and space, potential temperature variations can
171 be Taylor expanded to give (Corrsin (1974); Schneider et al. (2015))

$$\theta' \approx -\frac{\partial \bar{\theta}}{\partial y} L'_y - \frac{\partial \bar{\theta}}{\partial x} L'_x + \frac{1}{2} \frac{\partial^2 \bar{\theta}}{\partial y^2} L'^2 + \dots, \quad (2)$$

172 where $\theta' = \theta - \bar{\theta}$ denotes synoptic variations of potential temperature at 850hPa about some lo-
173 cal mean value $\bar{\theta}$, L'_y is the Lagrangian displacement of air masses arriving at y from y_0 , and
174 similarly for L'_x . “Mean” denotes an average over a time-scale that is long compared to synoptic
175 time-scales and we consider potential temperature rather than temperature because potential tem-
176 perature is materially conserved during adiabatic airmass displacements. We work in Cartesian
177 co-ordinates for simplicity, and define L'_y as positive for a northward displacement and L'_x as posi-
178 tive for an eastward displacement. Provided the length scales of potential temperature variations,
179 $\overline{L_y} = 2|\partial_y \bar{\theta} / \partial_{yy} \bar{\theta}|$ and $\overline{L_x} = 2|\partial_x \bar{\theta} / \partial_{xx} \bar{\theta}|$, are much larger than the mixing length-scales, L'_y and L'_x ,
180 the expansion can be well approximated by just retaining the first two terms, and so the synoptic
181 potential temperature variance can be approximated as

$$\overline{\theta'^2} \approx \overline{\left(\frac{\partial \bar{\theta}}{\partial y}\right)^2 L'^2_y} + \overline{\left(\frac{\partial \bar{\theta}}{\partial x}\right)^2 L'^2_x} + 2 \overline{\left(\frac{\partial \bar{\theta}}{\partial y}\right) L'_y \left(\frac{\partial \bar{\theta}}{\partial x}\right) L'_x}. \quad (3)$$

182 The meridional term, specifically the meridional temperature gradient, generally dominates over
183 the zonal term and the cross term, but we have included the latter two here to emphasize that zonal
184 temperature gradients also impact regional potential temperature variability.

185 Orography affects temperature gradients by meridionally compressing downstream near-surface
186 isentropes and pulling apart upstream isentropes. However, this requires the flow to be deflected

around the orography, rather than flowing up and over it, so that the air deflected equatorward
 partly adjusts to the warmer conditions and the air deflected poleward partly adjusts to the colder
 conditions, before the downstream confluence of the flow. For small heights the air flows up and
 over the orography, leaving the potential temperature gradients unaffected. Formally, consider the
 linearized, time-mean thermodynamic equation on the lowest model level (in z coordinates):

$$\bar{u} \frac{\partial \theta'}{\partial x} + v' \frac{\partial \bar{\theta}}{\partial y} = -w \frac{\partial \bar{\theta}}{\partial z}. \quad (4)$$

The orographic forcing enters through the lower boundary condition, which can be approximated
 as (Cook and Held 1992)

$$w \approx \bar{u} \frac{\partial h}{\partial x}, \quad (5)$$

where the forcings associated with the meridional wind and with zonal wind anomalies are ig-
 nored. Substituting then gives

$$\bar{u} \frac{\partial \theta'}{\partial x} + v' \frac{\partial \bar{\theta}}{\partial y} = -\bar{u} \frac{\partial h}{\partial x} \frac{\partial \bar{\theta}}{\partial z}. \quad (6)$$

If the air moves up and over the mountain then the first term on the left side of equation 6 balances
 the right side and $\frac{\theta'}{H} \sim \frac{\partial \bar{\theta}}{\partial z}$. For larger H , the deflection around the orography dominates, and the
 orographic forcing is balanced by the $v' \frac{\partial \bar{\theta}}{\partial y}$ term¹. In idealized experiments this transition occurs
 for H between 1 and 2km for orography with approximately the same horizontal extent as the
 Tibetan Plateau (Cook and Held (1992), Lutsko and Held (2016)). Valdes and Hoskins (1991)
 demonstrated that Asian topography meets this criterion, but caution that it is less clear whether
 the Rockies do: the near-surface flow appears to be deflected around the Rockies (see Figure 9

¹Though note that the potential temperature perturbation is itself proportional to the deflection of the flow: $\theta' \approx \eta' \frac{\partial \bar{\theta}}{\partial y}$, where η is the typical meridional displacement of a fluid parcel, assumed to be equal to the meridional extent of the orography. Hence for the meridional deflection to dominate $|\eta/H| < \left| \frac{\partial \bar{\theta}}{\partial z} / \frac{\partial \bar{\theta}}{\partial y} \right|$; i.e., the meridional slope of the mountain must be greater than the characteristic slope of the isentropes (Valdes and Hoskins 1991).

203 below), but this flow is strongly influenced by heating in the north Pacific storm track (see also
204 Valdes and Hoskins (1989)).

205 *b. Idealized GCM results*

206 In both idealized GCMs, temperature variance is reduced upstream and enhanced downstream
207 of orography (Figure 3a and b), as are meridional temperature gradients (panels c and d). However
208 the inferred mixing lengths $L' = \sqrt{\theta'^2 / \left(\frac{\partial \bar{\theta}}{\partial y}\right)^2}$ are reduced downstream of the orography (panels
209 e and f), which is the result of two competing effects. First, by increasing downstream temperature
210 gradients, orography increases downstream Eady growth rates, resulting in more energetic eddies
211 and thus to larger mixing lengths (see Caballero and Hanley (2012) for discussion of the rela-
212 tionship between eddy kinetic energy and mixing lengths). But in addition to local baroclinicity,
213 eddies in strong jets are also energized by downstream development – by the recycling of energy
214 from upstream eddies (Chang and Orlanski (1993); Chang et al. (2002)). Orography disrupts the
215 latter by interfering with the zonal propagation of wave packets (Son et al. 2009), and for the set-
216 ups used here this effect wins out, resulting in less energetic eddies and smaller effective mixing
217 lengths.

218 Nevertheless, the enhanced meridional temperature gradients cause a local enhancement of tem-
219 perature variance downstream of the orography in both models. Figure 4 shows that the maximum
220 zonal anomaly in potential temperature variance increases in the simulations with the dry and
221 moist GCMs as the height of the orography (H) is increased (panel a²), as does the maximum
222 zonal anomaly of the squared meridional temperature gradient (panel b). Plotting these against
223 each other demonstrates the strong linear relationship between the two quantities in these GCMs

2Note that the zonal-mean variance decreases with increasing H because of the increasing disruption of downstream development by the orography (not shown).

224 (panel c). The different slopes indicate that the mixing lengths differ in the two models, and the
225 larger slope for the moist GCM implies that adding moist processes increases the effective mixing
226 length (see below).

227 A possible complication is the shape of the orography: the Rockies form a meridionally-
228 elongated ridge, whereas the Himalayas are more zonally-elongated. To investigate how the orog-
229 raphy's shape influences temperature variability, two additional simulations were run with the dry
230 GCM, one with a 4km meridional ridge resembling the Rockies ($\alpha = 15^\circ$ and $\beta = 5^\circ$) and one
231 with a 4km zonal ridge, resembling the Himalayas ($\alpha = 5^\circ$ and $\beta = 15^\circ$). Figure 5 shows that the
232 patterns of anomalous variability are similar in these cases to the circular mountain, and thus the
233 shape of the mountain seems to be of secondary importance for synoptic temperature variability.

234 In the dry GCM, advection is the sole method of generating potential temperature variance,
235 whereas in the moist GCM covariance of anomalous latent heating and potential temperature
236 anomalies also contributes. To investigate the role of latent heat anomalies, Figure 6 shows the ad-
237 vective terms in the temperature variance budget (see equation 3 of Wilson and Williams (2006))
238 for the 4km simulation with the moist GCM, as well as the contribution of latent heat fluctuations
239 to temperature variance (Figure 6d). Latent heating enhances temperature variability downstream
240 of the orography, however this enhancement is less than 20% of the advective tendency, which is
241 dominated by the $\overline{\mathbf{u}'\theta' \cdot \nabla \bar{\theta}}$ term. So we can ignore the latent heating term $\overline{\theta' Q'_L}$ to first-order, but
242 note that it increases the effective mixing lengths diagnosed in the moist GCM.

243 **4. Temperature Variability in Simulations with Flattened Orography**

244 Figure 7a shows that FLOR is able to reproduce the main features of the observed pattern of
245 DJF synoptic temperature variance³. Flattening Asian orography increases the temperature vari-
246 ance over most of Eurasia, as well as over North America (panel b of Figure 7, Figure 8), while
247 flattening the Rockies reduces the variance over most of North America but increases it off the
248 west coast of North America (panel c of Figure 7, Figure 8). Table 1 quantifies the changes in
249 temperature variance over the two continents by comparing DJF synoptic temperature variance
250 in the three FLOR simulations over a Eurasian box (40° - 120° E and 30° - 75° N) and over a North
251 American box (240° - 280° E and 30° - 75° N). The areas of the Asian mountains and the Rockies
252 are masked whenever an average is taken over these boxes. The variance over the Eurasian box
253 is increased by 1.4K^2 and the variance over North America is increased by 1.3K^2 in the no-Tibet
254 simulation, and both of these changes are statistically significant at the 95% level based on a two-
255 sided Student's t-test. In the no-Rockies simulation the variance over North America is reduced
256 by 1.3K^2 and the variance over Eurasia is reduced by 0.2K^2 . Only the change over North America
257 is statistically significant in this case.

258 These calculations suggest that the enhancement of North American temperature variability by
259 the Rockies is roughly cancelled by the damping of variability due to Asian orography. We note,
260 however, that the increases and decreases in variance are sensitive to the definitions of the boxes,
261 and that this cancellation also assumes the effects of flattening the mountain ranges individually
262 can be linearly added together. Regardless, the majority of the orography's net effect comes from
263 the reduction of Eurasian temperature variability by the Asian mountains and, in FLOR, this ex-
264 plains about a quarter of the difference in variance over the two continents ($1.4\text{K}^2 / 5.5\text{K}^2 \approx 25\%$).

³The temperature variance is somewhat higher in the FLOR simulations than in the reanalysis, which we attribute to the higher resolution of FLOR's atmospheric model compared to the reanalysis.

265 The remaining difference comes from stationary waves forced by diabatic heating, as even in the
266 no-Rockies simulation there are substantial meridional temperature gradients over North America
267 (Figure 7f). Moreover, the stationary wave pattern over North America is similar in all three sim-
268 ulations, consisting of a dipole with anomalously warm temperatures off the west coast of North
269 America and anomalously cold temperatures centered over northeast Canada (Figure 7 panels g),
270 h) and i)). The dipole is weaker in the no-Rockies simulation, indicating that the stationary wave
271 forced by the Rockies constructively interferes with the dipole. In this case, the pattern over
272 North America is a combination of the stationary wave forced by the land-sea contrast between
273 the east coast of North America and the western Atlantic (Kaspi and Schneider 2011), which cools
274 eastern North America, and stationary waves forced by diabatic heating in the Pacific warm pool
275 region and by thermal forcing in the extratropical Pacific (Hoskins and Karoly (1981); Valdes and
276 Hoskins (1991); Held et al. (2002)). The latter includes the forcing due to the warm waters of the
277 Kuroshio as well as the eddy sensible heat flux convergence in the Pacific storm track, making it
278 difficult to separate out the relative contributions of the different thermal forcings.

279 The dipole over North America is weakly affected by flattening Tibet, and these small changes
280 in temperature gradients are unlikely to have a major impact on temperature variability over North
281 America. Instead, the main reason for the enhanced North American variability in the no-Tibet
282 simulation is Tibet's interference with downstream development. The Kuroshio Extension off the
283 east coast of Japan is the genesis region for the Pacific storm track, and flattening the Himalayas
284 and Tibet strengthens the eddies formed over the Kuroshio because of the additional energy from
285 upstream (Figure 10). So although the temperature gradient in the northwest Pacific is reduced
286 without the orography, the temperature variance is increased (panel b of Figure 7 and panel b of
287 Figure 8), and the enhanced downstream development also impacts the strength of winter storms
288 originating in the Pacific storm track and reaching North America.

289 Over eastern and central Eurasia, the dominant feature in winter is anomalous cold due to the
290 stationary wave excited by the land-sea contrast on Eurasia's east coast (Kaspi and Schneider
291 2011). This cold weakens in the no-Tibet simulation, as the stationary wave forced by the Asian
292 orography constructively interferes with the land-sea wave (see also Park et al. (2013)). Further-
293 more, the largest temperature gradients in the no-Tibet simulation are at relatively low latitudes,
294 at about 30°N. Since the mid-latitude jet, where the mixing lengths are largest, is further north,
295 the southward displacement of the maximum temperature gradient further reduces temperature
296 variance over Eurasia compared to North America.

297 Finally, we note that temperature variance over the southeast Asian coast, including parts of
298 southern China, is enhanced in the no-Tibet run, despite this region being east of the Himalayas.
299 But at these latitudes the zonal-winds transition from westerly to easterly and this region is, in
300 part, upstream of the orography (Figure 9). Thus an enhancement of variability is expected when
301 the Himalayas and Tibet are flattened.

302 **5. Temperature Skewness**

303 Through its effects on temperature gradients, orography also impacts the skewness of synoptic
304 temperatures. Garfinkel and Harnik (2017) showed that, in mid-latitudes, synoptic temperature
305 extremes can occur when air is advected over regions with large mean meridional temperature
306 gradients, so that temperatures poleward of these regions tend to be positively skewed and temper-
307 ature equatorward of these regions tend to be negatively skewed. By strengthening downstream
308 temperature gradients, orography increases the positive skewness to the north of these gradients
309 and the negative skewness to the south. This is illustrated in Figure 11, which shows maps of
310 skewness in simulations with the two idealized GCMs, as well as the meridional temperature gra-

311 dients. In both cases, downstream temperatures are skewed more positively north of the enhanced
312 temperature gradients and more negatively to the south of the gradients.

313 In the reanalysis data, the strongest DJF meridional temperature gradients are found in the storm
314 track regions of the west Pacific and the west Atlantic (Figure 1c). Panel a of Figure 12 shows that
315 synoptic temperatures are positively skewed in the northwest Pacific and the northwest Atlantic,
316 and negatively skewed to the south of these regions. The same patterns are seen in the control
317 simulation with FLOR (Figure 12b, note that as with the variance, we attribute the larger values
318 of skewness to FLOR's higher resolution). The temperature gradient in the west Pacific is reduced
319 in the no-Tibet simulation, and comparing panels b and c of Figure 12 confirms that the skewness
320 in the northwest Pacific is also reduced in this simulation. Averaging over the region 35°N-50°N
321 and 140°E to 180°E (green box in Figure 12b) gives a reduction in skewness of 31% (= (0.234 -
322 0.162) / 0.234, difference significant at the 90% level) in the northwest Pacific.

323 Temperature gradients in the west Atlantic are affected little by flattening the Rockies (Figure
324 7f), and the skewness in the northwest Atlantic is comparable in the control and the no-Rockies
325 simulations. Over land, DJF synoptic temperatures are negatively skewed at almost all latitudes,
326 and other factors, such as land-surface feedbacks, are likely important for generating extreme
327 events.

328 6. Conclusion

329 In this study we have investigated the contribution of large-scale orography to the increased win-
330 tertime near-surface daily and synoptic temperature variability over North America compared to
331 Eurasia. Our analysis combines theoretical arguments, simulations with two idealized GCMs and
332 simulations with a comprehensive climate model – GFDL CM2.5-FLOR – in which the Rockies
333 and the Asian orography are separately flattened. These allow us to quantify the impacts these

334 mountain ranges have on temperature variability over North America and Eurasia, and suggest
335 that large-scale Northern Hemisphere orography is responsible for roughly 25% of the difference
336 in variability.

337 Large-scale orography enhances downstream temperature variability by meridionally compress-
338 ing downstream isentropes, while upstream temperature variability is reduced because upstream
339 isentropes are pulled apart. Most of North America is downstream of the Rockies, so wintertime
340 temperature variability is enhanced there, while the Asian orography is on the eastern edge of
341 Eurasia, so temperature variability is damped over most of Eurasia. An important exception is the
342 southeast Asian littoral, which is east of the orography but exhibits reduced temperature variability
343 due to the Asian mountains. These regions are at latitudes of mean easterlies, or in the transition
344 from mean westerlies to mean easterlies, and hence are also upstream of the Himalayas. At the
345 same time, Asian orography interferes with the energization of eddies in the Pacific storm track by
346 downstream development, resulting in weaker winter storms and hence damping variability over
347 North America. This reduction in variability is approximately as large as the increase in variability
348 due to the presence of the Rockies.

349 We have also shown that orography enhances downstream skewness, as regions to the north of
350 the enhanced temperature gradient have more positively skewed temperatures and regions to the
351 south have more negatively skewed temperatures. In the FLOR simulations, the Himalayas and
352 the Tibetan Plateau are found to increase temperature skewness in the northwest Pacific by about
353 30%.

354 The remaining difference in synoptic temperature variability over North America compared to
355 Eurasia is primarily due to a combination of diabatic heating in the Pacific warm pool region,
356 air-sea fluxes over the warm Kuroshio current and eddy sensible heat flux convergence in the Pa-
357 cific storm track. The smaller width of the North American continent and its northwest-southeast

358 sloping western coastline may also be important – Brayshaw et al. (2009) explored how this in-
359 fluences the North Atlantic storm track. Separating out these different factors, and the non-linear
360 interactions between them, is an important next step.

361 The dominant control of horizontal advection on winter synoptic temperature variability is a
362 powerful tool for understanding the regional pattern of temperature variability, in today's climate
363 and how it may change in the future. This simplifies the problem to understanding the boreal winter
364 stationary wave pattern, for which there is a large body of literature which can be drawn on (e.g.,
365 Hoskins and Karoly (1981); Held (1983); Held et al. (2002)), though differences in mixing lengths,
366 for instance due to orographic interference with downstream development, are an important caveat.
367 Similarly, past and future changes in temperature variability can potentially be tied to changes in
368 the stationary wave pattern (see e.g., Löfverström et al. (2014) and Simpson et al. (2016) for
369 investigations of past and future changes in Northern Hemisphere stationary waves). More work
370 is needed to better understand the impact of orography on mixing lengths, as well as to account
371 for land surface processes such as soil-moisture, which affect temperature variability, particularly
372 during summer. These factors are also important for temperature extremes, particularly over land,
373 where winter temperatures at almost all latitudes are negatively skewed. Nevertheless, the basic
374 dynamics we describe here are robustly seen in idealized GCMs and in comprehensive climate
375 models, and provide an important first step in explaining why North America experiences more
376 wintertime temperature variability than Eurasia.

377 *Acknowledgment.* We thank Daniel Koll, Rodrigo Caballero and Gabriel Vecchi for helpful con-
378 versations over the course of this work. The manuscript also benefited from feedback from Daniel
379 Koll and Paul O'Gorman on earlier drafts, and Gabriel Vecchi kindly provided the computational
380 resources to perform the FLOR simulations. This work was partly supported by NSF grant AGS-

381 1623218, “Collaborative Research: Using a Hierarchy of Models to Constrain the Temperature
382 Dependence of Climate Sensitivity”.

383 **References**

- 384 Barnes, E. A., and L. M. Polvani, 2015: Cmip5 projections of arctic amplification, of the north
385 american/north atlantic circulation, and of their relationship. *Journal of Climate*, **28** (3), 5254–
386 5271.
- 387 Bathiany, S., V. Dakos, M. Scheffer, and T. M. Lenton, 2018: Climate models predict increasing
388 temperature variability in poor countries. *Science Advances*, **4** (5).
- 389 Bowers, E. K., J. L. Grindstaff, S. S. Soukup, N. E. Drilling, K. P. Eckerle, S. K. Sakaluk, and C. F.
390 Thompson, 2016: Spring temperatures influence selection on breeding date and the potential for
391 phenological mismatch in a migratory bird. *Ecology*, **97**, 2880–2891.
- 392 Brayshaw, D. J., B. Hoskins, and M. Blackburn, 2009: The basic ingredients of the north at-
393 lantic storm track. part i: Landsea contrast and orography. *Journal of the Atmospheric Sciences*,
394 **66** (23), 2539–2558.
- 395 Caballero, R., and J. Hanley, 2012: Midlatitude eddies, storm-track diffusivity, and poleward
396 moisture transport in warm climates. *Journal of the Atmospheric Sciences*, **69** (630), 3237–
397 3250.
- 398 Chang, E. K. M., S. Lee, and K. L. Swanson, 2002: Storm track dynamics. *Journal of Climate*,
399 **15** (16), 2163–2183.
- 400 Chang, E. K. M., and I. Orlanski, 1993: On the dynamics of a storm track. *Journal of the Atmo-*
401 *spheric Sciences*, **50** (56), 999–1015.

- 402 Cohen, J., and Coauthors, 2014: Recent arctic amplification and extreme mid-latitude weather.
- 403 *Nature Geoscience*, **7**, 627–637.
- 404 Cook, K. H., and I. M. Held, 1992: The stationary response to large-scale orography in a general
- 405 circulation model and a linear model. *Journal of the Atmospheric Sciences*, **49** (6), 525–539.
- 406 Corrsin, S., 1974: Limitations of gradient transport models in random walks and in turbulence.
- 407 *Advances in Geophysics*, **18A**, 25–60.
- 408 Frierson, D. M. W., 2007: The dynamics of idealized convection schemes and their effect on the
- 409 zonally averaged tropical circulation. *Journal of the Atmospheric Sciences*, **64** (23), 1959–1976.
- 410 Frierson, D. M. W., I. M. Held, and P. Zurita-Gotor, 2006: A gray-radiation aquaplanet moist gcm.
- 411 part i: Static stability and eddy scales. *Journal of the Atmospheric Sciences*, **63** (23), 2548–2566.
- 412 Garfinkel, C. I., and N. Harnik, 2017: The non-gaussianity and spatial asymmetry of temperature
- 413 extremes relative to the storm track: The role of horizontal advection. *Journal of Climate*, **30**,
- 414 445–464.
- 415 Held, I. M., 1983: Stationary and quasi-stationary eddies in the extratropical troposphere: theory.
- 416 *Large-scale Dynamical Processes in the Atmosphere*, B. J. Hoskins, and R. P. Pearce, Eds.,
- 417 Academic Press, New York, NY.
- 418 Held, I. M., and M. J. Suarez, 1994: A proposal for the intercomparison of the dynamical cores
- 419 of atmospheric general circulation models. *Bulletin of the American Meteorological Society*,
- 420 **75** (10), 1825–1830.
- 421 Held, I. M., M. Ting, and H. Wang, 2002: Northern winter stationary waves: Theory and modeling.
- 422 *Journal of Climate*, **15** (16), 2125–2144.

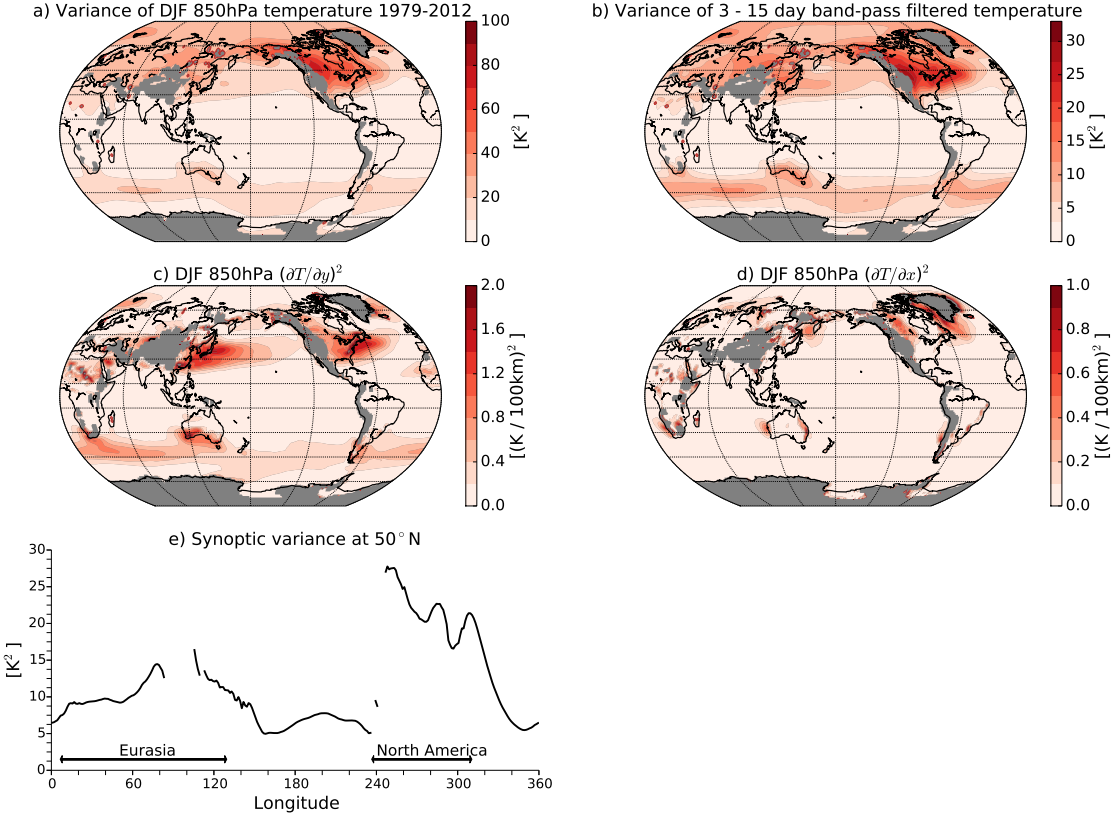
- 423 Holmes, C. R., T. Woollings, E. Hawkins, and H. de Vries, 2016: Robust future changes in tem-
424 perature variability under greenhouse gas forcing and the relationship with thermal advection.
425 *Journal of Climate*, **29** (29), 2221–2235.
- 426 Hoskins, B., and T. Woollings, 2015: Persistent extratropical regimes and climate extremes. *Cur-*
427 *rent Climate Change Reports*, **1** (3), 115–124.
- 428 Hoskins, B. J., and D. J. Karoly, 1981: The steady linear response of a spherical atmosphere to
429 thermal and orographic forcing. *Journal of the Atmospheric Sciences*, **38** (6), 1179–1196.
- 430 Huybers, P., K. A. McKinnon, A. Rhines, and M. Tingley, 2014: U.s. daily temperatures: The
431 meaning of extremes in the context of nonnormality. *Journal of Climate*, **27**, 7368–7384.
- 432 Jackson, S. T., J. L. Betancourt, R. K. Booth, and S. T. Gray, 2009: Ecology and the ratchet
433 of events: Climate variability, niche dimensions, and species distributions. *Proceedings of the*
434 *National Academy of Sciences*, **106**, 19 685–19 692.
- 435 Jahn, M., 2015: Economics of extreme weather events: Terminology and regional impact models.
436 *Weather and Climate Extremes*, **10**, 29 – 39.
- 437 Kaspi, Y., and T. Schneider, 2011: Winter cold of eastern continental boundaries induced by warm
438 ocean waters. *Nature*, **472**, 621–624.
- 439 Lau, N.-C., and M. J. Nath, 2012: A model study of heat waves over north america: Meteorological
440 aspects and projections for the twenty-first century. *Journal of Climate*, **25**, 4761–4784.
- 441 Lau, N.-C., and M. J. Nath, 2014: Model simulation and projection of european heat waves in
442 present-day and future climates. *Journal of Climate*, **27**, 3713–3730.
- 443 Lazo, J. K., M. Lawson, P. H. Larsen, and D. M. Walkman, 2011: U.s. economic sensitivity to
444 weather variability. *Bulletin of the American Meteorological Society*, **92** (29), 709–720.

- 445 Linz, M., G. Chen, and Z. Hu, 2018: Large-scale atmospheric control on non-gaussian tails of
446 midlatitude temperature distributions. *Geophysical Research Letters*, **45** (15), 9141–9149.
- 447 Löfverström, M., R. Caballero, J. Nilsson, and J. Kleman, 2014: Evolution of the large-scale
448 atmospheric circulation in response to changing ice sheets over the last glacial cycle. *Climate of
449 the Past*, **10** (4), 1453–1471.
- 450 Lutsko, N. J., and I. M. Held, 2016: The response of an idealized atmosphere to orographic
451 forcing: Zonal versus meridional propagation. *Journal of the Atmospheric Sciences*, **73** (9),
452 3701–3718.
- 453 McKinnon, K. A., A. Rhines, M. Tingley, and P. Huybers, 2016: The changing shape of northern
454 hemisphere summer temperature distributions. *Journal of Geophysical Research: Atmospheres*,
455 **121**, 8849–8868.
- 456 O’Gorman, P. A., and T. Schneider, 2008: The hydrological cycle over a wide range of climates
457 simulated with an idealized gcm. *Journal of Climate*, **21** (15), 3815–3832.
- 458 Park, H.-S., S.-P. Xie, and S.-W. Son, 2013: Poleward stationary eddy heat transport by the tibetan
459 plateau and equatorward shift of westerlies during northern winter. *Journal of the Atmospheric
460 Sciences*, **70** (23), 3288–3301.
- 461 Rahmstorf, S., and D. Coumou, 2011: Increase of extreme events in a warming world. *Proceedings
462 of the National Academy of Sciences*, **108** (44), 17 905–17 909.
- 463 Rienecker, M. M., and Coauthors, 2011: Merra: Nasa’s modern-era retrospective analysis for
464 research and applications. *Journal of Climate*, **24**, 3624–3648.
- 465 Schneider, T., T. Bischoff, and H. Plotka, 2015: Physics of changes in synoptic midlatitude tem-
466 perature variability. *Journal of Climate*, **28** (6), 2312–2331.

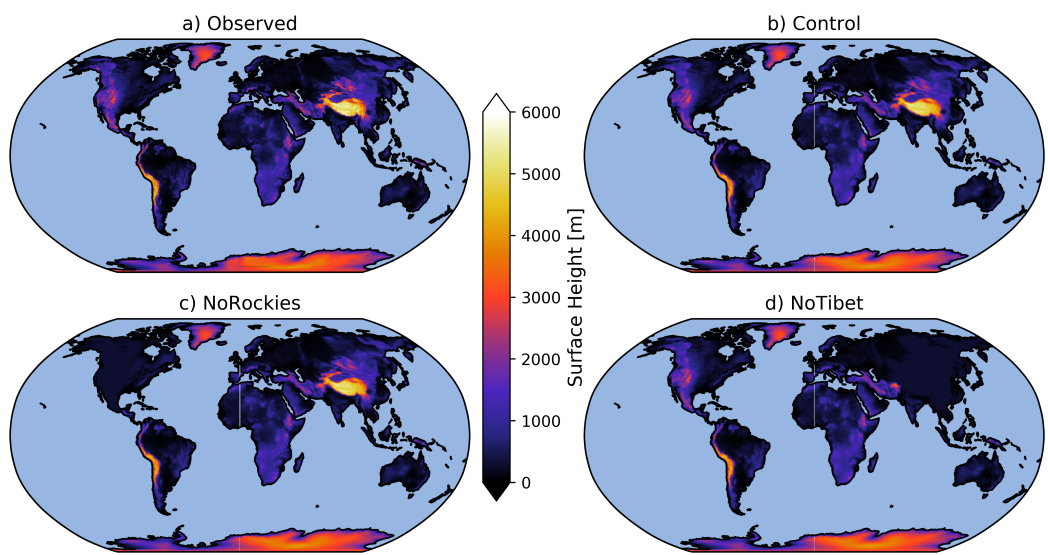
- 467 Screen, J. A., 2014: Arctic amplification decreases temperature variance in northern mid- to high-
468 latitudes. *Nature Climate Change*, **4**, 577–582.
- 469 Shi, L., I. Kloog, A. Zanobetti, P. Liu, and J. D. Schwartz, 2015: Impacts of temperature and its
470 variability on mortality in new england. *Nature Climate Change*, **5**, 988–991.
- 471 Simpson, I. R., R. Seager, M. Ting, and T. A. Shaw, 2016: Causes of change in northern hemi-
472 sphere winter meridional winds and regional hydroclimate. *Nature Climate Change*, **6**, 65–70.
- 473 Son, S.-W., M. Ting, and L. M. Polvani, 2009: The effect of topography on storm-track intensity
474 in a relatively simple general circulation model. *Journal of the Atmospheric Sciences*, **66** (23),
475 393–311.
- 476 Valdes, P. J., and B. J. Hoskins, 1989: Linear stationary wave simulations of the time-mean clima-
477 tological flow. *Journal of the Atmospheric Sciences*, **46** (18), 2509–2527.
- 478 Valdes, P. J., and B. J. Hoskins, 1991: Nonlinear orographically forced planetary waves. *Journal*
479 *of the Atmospheric Sciences*, **48** (18), 2089–2106.
- 480 Vecchi, G. A., and Coauthors, 2014: On the seasonal forecasting of regional tropical cyclone
481 activity. *Journal of Climate*, **27** (1), 7994–8016.
- 482 Wheeler, T., and J. von Braun, 2013: Climate change impacts on global food security. *Science*,
483 **341** (6145), 508–513.
- 484 Wills, R. C., and T. Schneider, 2018: Mechanisms setting the strength of orographic rossby waves
485 across a wide range of climates in a moist idealized gcm. *Journal of Climate*, **31** (18), 7679–
486 7700.
- 487 Wilson, C., and R. G. Williams, 2006: When are eddy tracer fluxes directed downgradient? *Jour-*
488 *nal of Physical Oceanography*, **36** (23), 189–202.

489 TABLE 1. Variance of December-January-February (DJF) 850hPa synoptic temperature over Eurasia (40°E -
 490 120°E and 30°N - 75°N) and North America (240°E - 280°E and 30°N - 75°N) in the FLOR simulations and ob-
 491 served variances from 1979-2012. All units are K^2 and the plus/minus values show the standard deviations of
 492 the interannual variability.

	MERRA reanalysis 1979-2012	Control	no-Tibet	no-Rockies
North America	15.7 ± 2.6	18.1 ± 2.4	19.4 ± 2.7	16.8 ± 2.9
Eurasia	8.6 ± 2.0	12.6 ± 2.3	14.0 ± 2.8	12.4 ± 2.2
Difference	7.1	5.5	5.4	4.4



493 FIG. 1. a) Variance of December-January-February (DJF) 850hPa daily temperature for the period 1979 to
 494 2012, calculated using data taken from the MERRA re-analysis dataset. Locations where topography intrudes
 495 through 850hPa are masked in gray. b) Same as panel a, but the data are filtered using a fourth-order Butterworth
 496 filter to only retain power at synoptic time-scales, here defined as 3 to 15 days. c) Climatological DJF squared
 497 meridional temperature gradients for the same data. d) Climatological DJF squared zonal temperature gradients
 498 for the same data. e) Profile of synoptic-scale 850hPa temperature variance at 50°N. Gaps in the profiles show
 499 where topography intrudes into the 850hPa level.



500 FIG. 2. a) Observed topography of Earth, taken from the ETOPO5 dataset, with 5 minute resolution. b)
 501 Topography in the control simulation of FLOR. c) Topography in the no-Rockies simulation. d) Topography in
 502 the no-Tibet simulation.

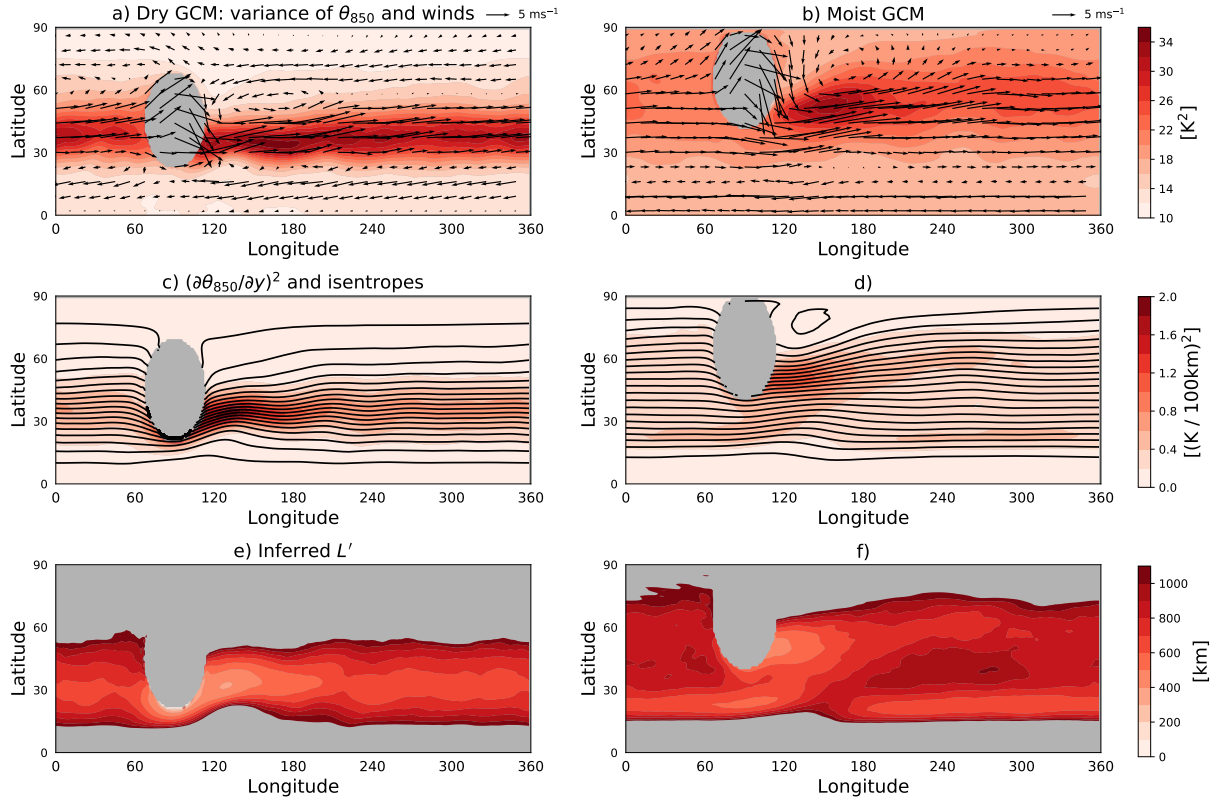
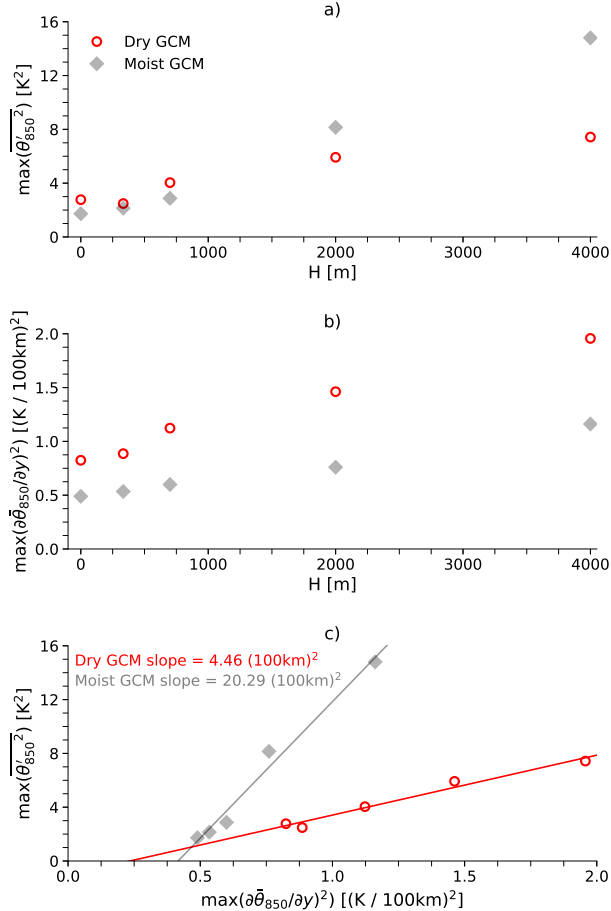
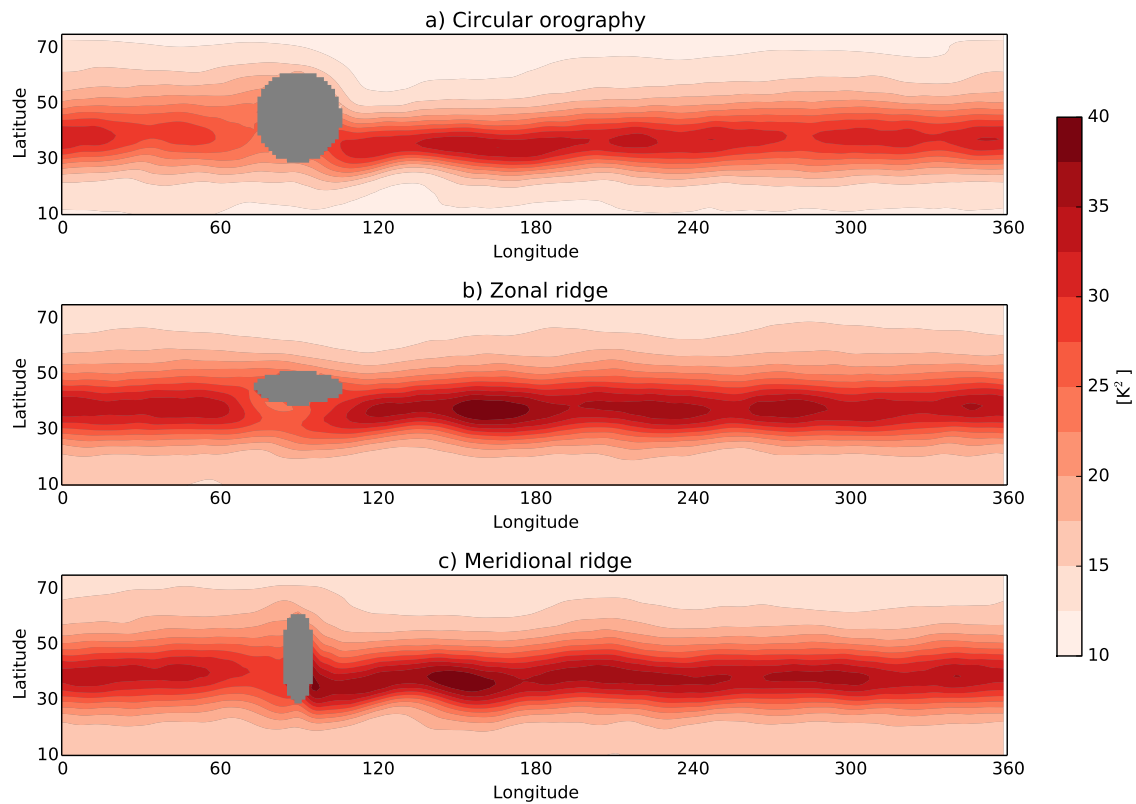


FIG. 3. a) Variance of synoptic (3 to 15 days) 850hPa potential temperature (contours) and total wind vectors (arrows) in a simulation with the dry GCM and maximum orographic height of 4km. b) Same as panel a) but for the simulation with the moist GCM with 4km orography. c) Squared meridional gradient of time-averaged potential temperature (colored contours) and isentropes (black contours, with contour interval 2K) at 850hPa for the same simulation as in panel a). d) Same as panel c) but for the simulation with the moist GCM with 4km orography. e) Inferred mixing length L' for the simulation with the dry GCM and maximum orographic height of 4km. f) Same as panel d) but for the simulation with the moist GCM with 4km orography. In all panels gray indicates locations with surface pressure less than 850hPa or, in the bottom panels, where values are outside the colorbar range. In a) and b) the winds are taken from the 0.85- σ level so that the flow over and around the orography is visible.



513 FIG. 4. a) Maximum anomalous 850hPa potential temperature variance ($\max(\bar{\theta}'_{850}^2)$) as a function of moun-
 514 tain height, H , in the simulations with the dry GCM (red circles) and with the moist GCM (gray diamonds).
 515 $\max(\bar{\theta}'_{850}^2)$ is calculated as the maximum zonal anomaly in 850hPa potential temperature variance in the 120°
 516 downstream of the peak of the orography. b) Maximum zonal anomaly of the squared meridional potential tem-
 517 perature gradient at 850hPa ($\max((\partial \bar{\theta}_{850}/\partial y)^2)$) as a function of H in the simulations with the idealized GCMs.
 518 $\max((\partial \bar{\theta}_{850}/\partial y)^2)$ is calculated as the maximum zonal anomaly in the 850hPa meridional potential temperature
 519 gradient in the 120° downstream of the peak of the orography. c) $\max(\bar{\theta}'_{850}^2)$ versus $\max((\partial \bar{\theta}_{850}/\partial y)^2)$ in the
 520 simulations with the idealized GCMs. The lines show linear least-squares fits to the two sets of simulations.



521 FIG. 5. a), b), c) Variance of synoptic (3-15 day) 850hPa potential temperature in the dry GCM simulations
 522 with $H = 4\text{km}$ and the circular Gaussian orography ($\alpha = \beta$) (a), the zonal ridge (b) and the meridional ridge (c).

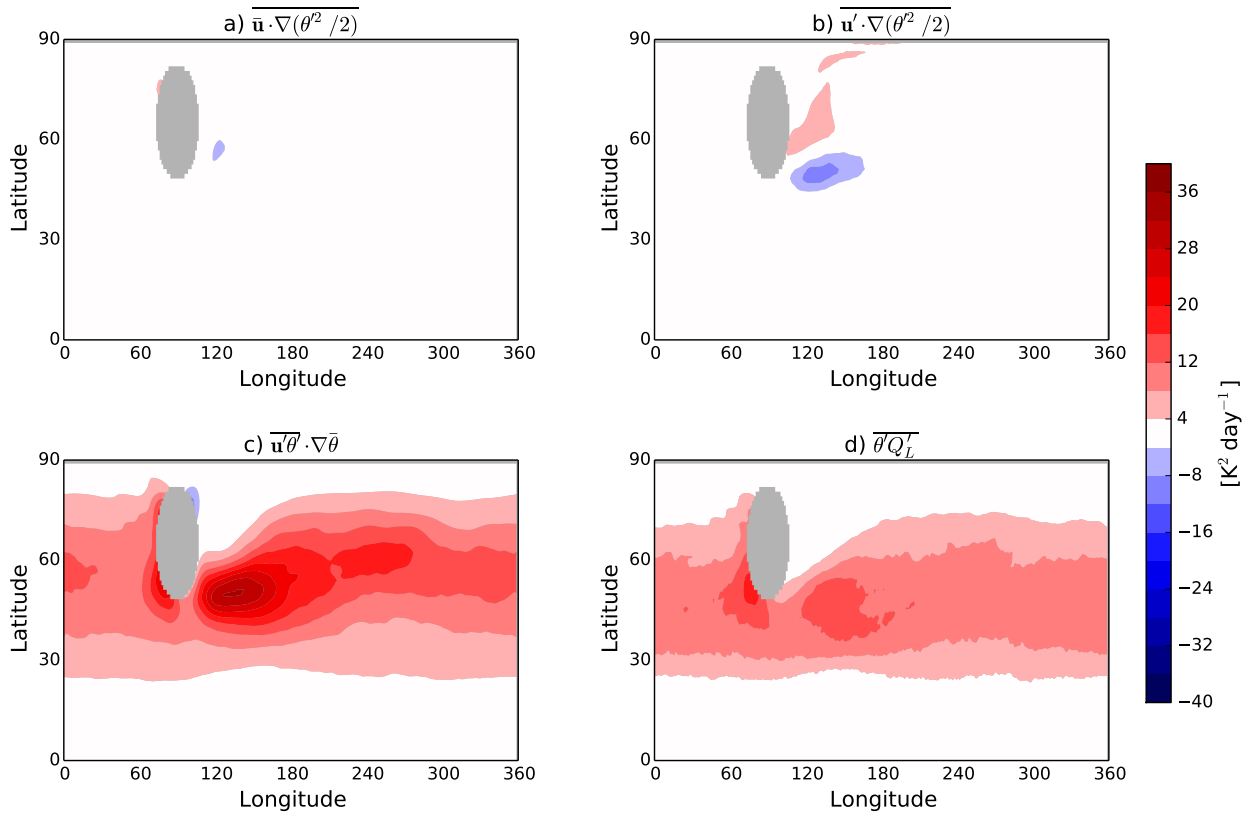
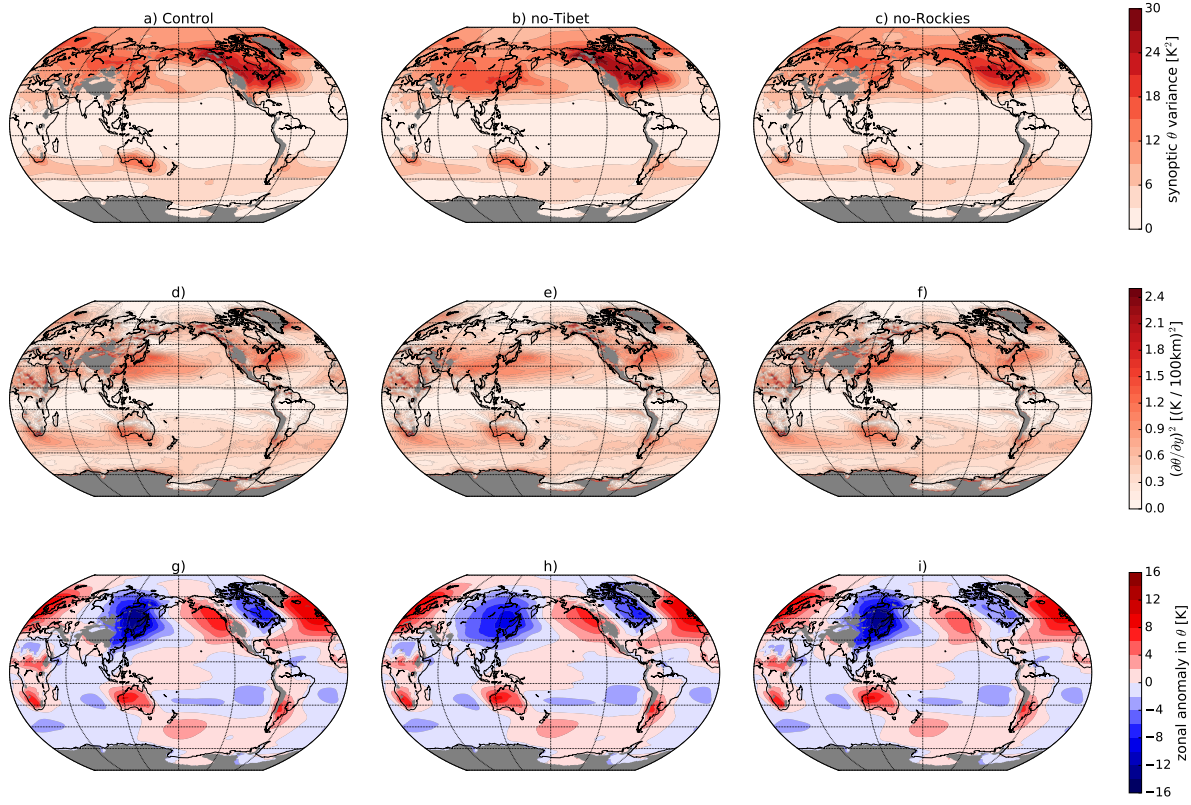
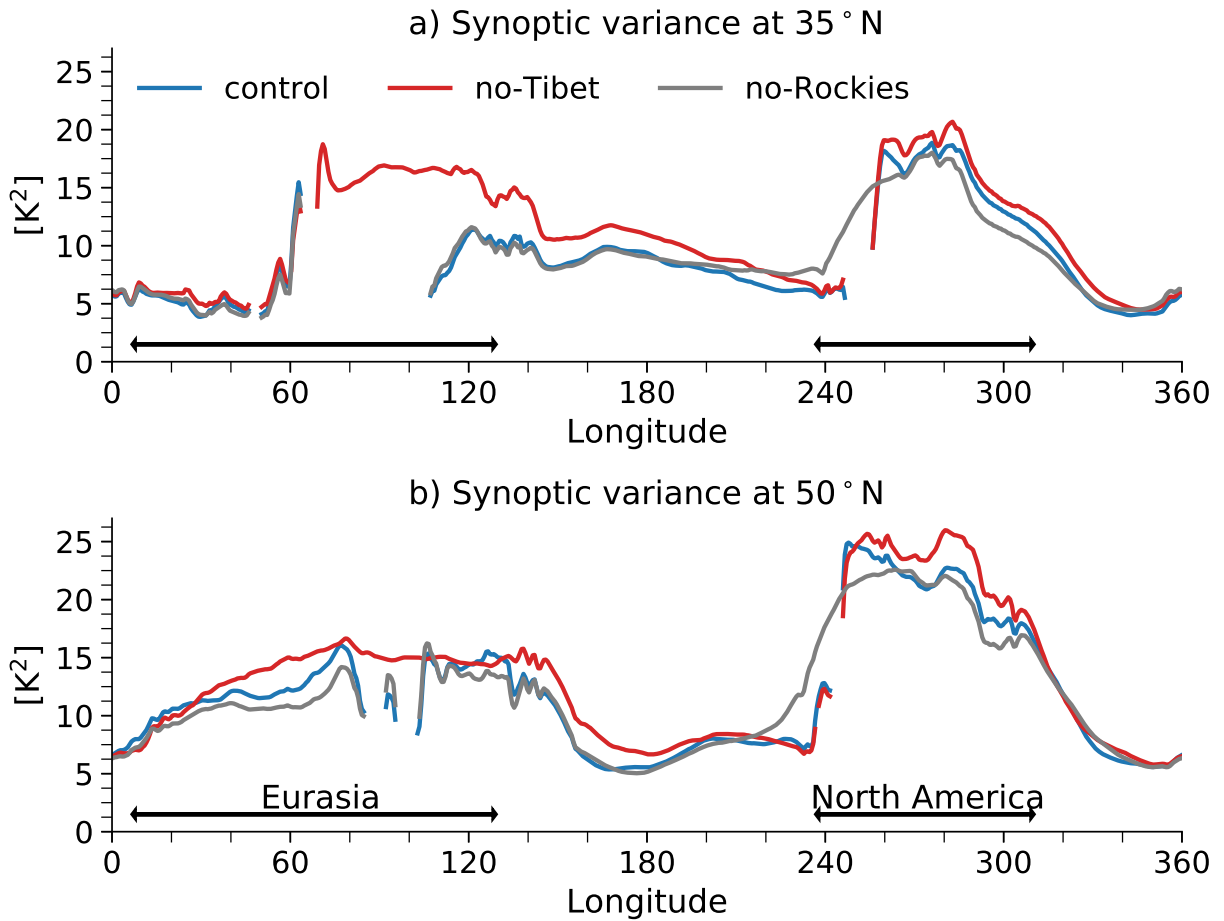


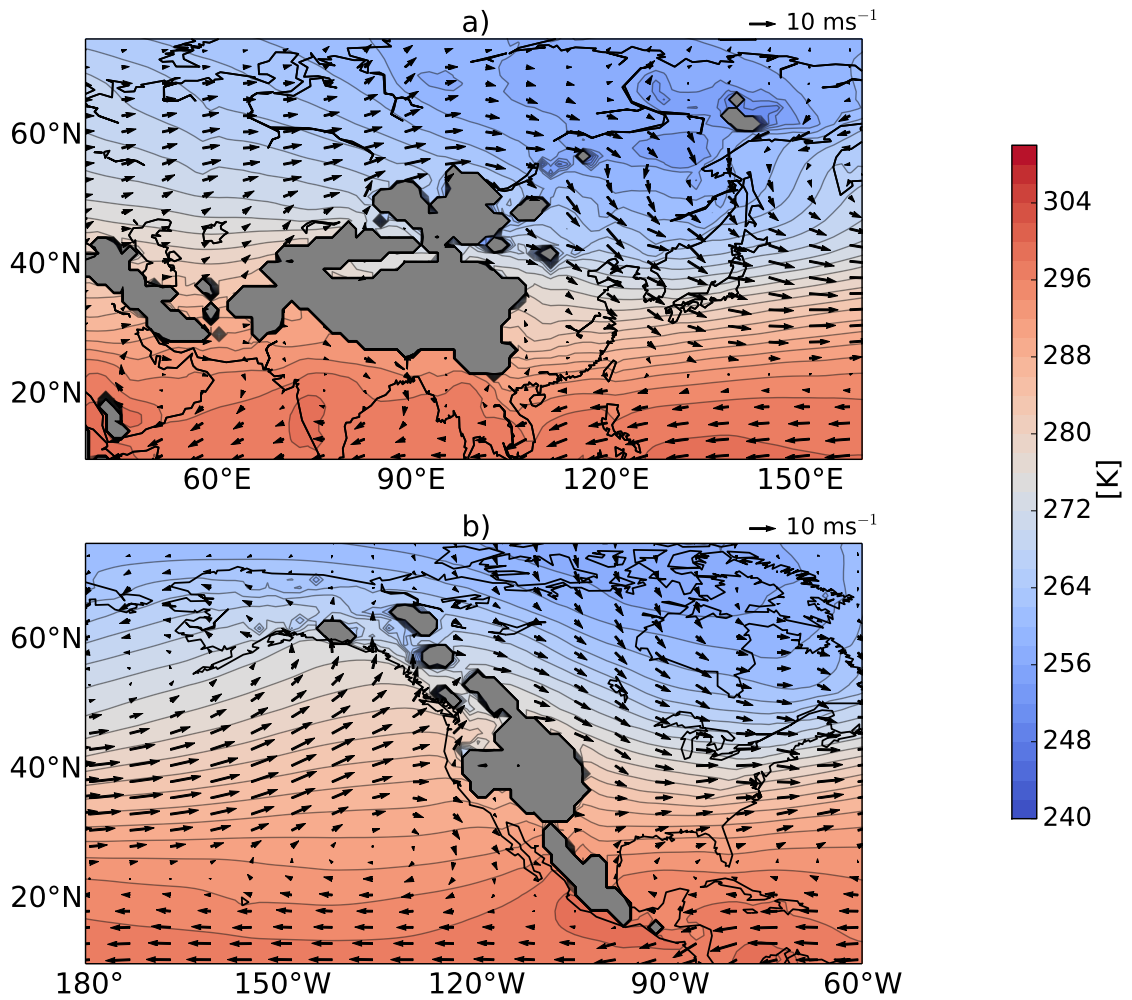
FIG. 6. Panels a), b) and c): advective terms in the 850hPa potential temperature variance budget from a simulation with the moist GCM and a mountain height of 4km. Locations where topography intrudes through 850hPa are masked in gray. Panel d): the contribution of latent heating fluctuations to 850hPa potential temperature variance in the same simulation.



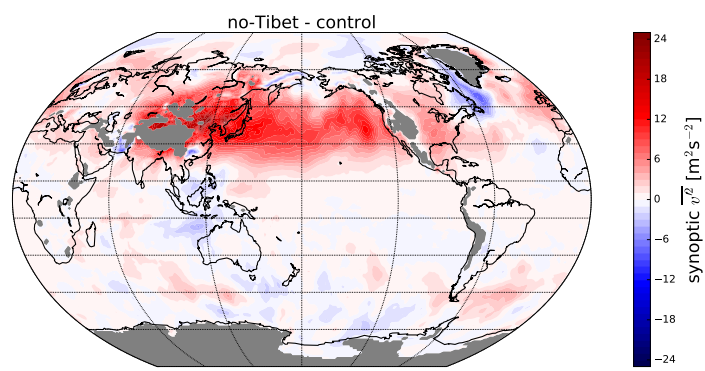
527 FIG. 7. a), b), c) Synoptic-scale variance of DJF 850hPa potential temperature in the control simulation
 528 with the comprehensive climate model, FLOR (a), the no-Tibet simulation (b) and the no-Rockies simulation
 529 (c). d), e), f) DJF squared meridional potential temperature gradients in the same simulations. g), h), i) DJF
 530 zonal anomalies in 850hPa potential temperature in the same simulations. Locations where topography intrudes
 531 through 850hPa are masked in gray.



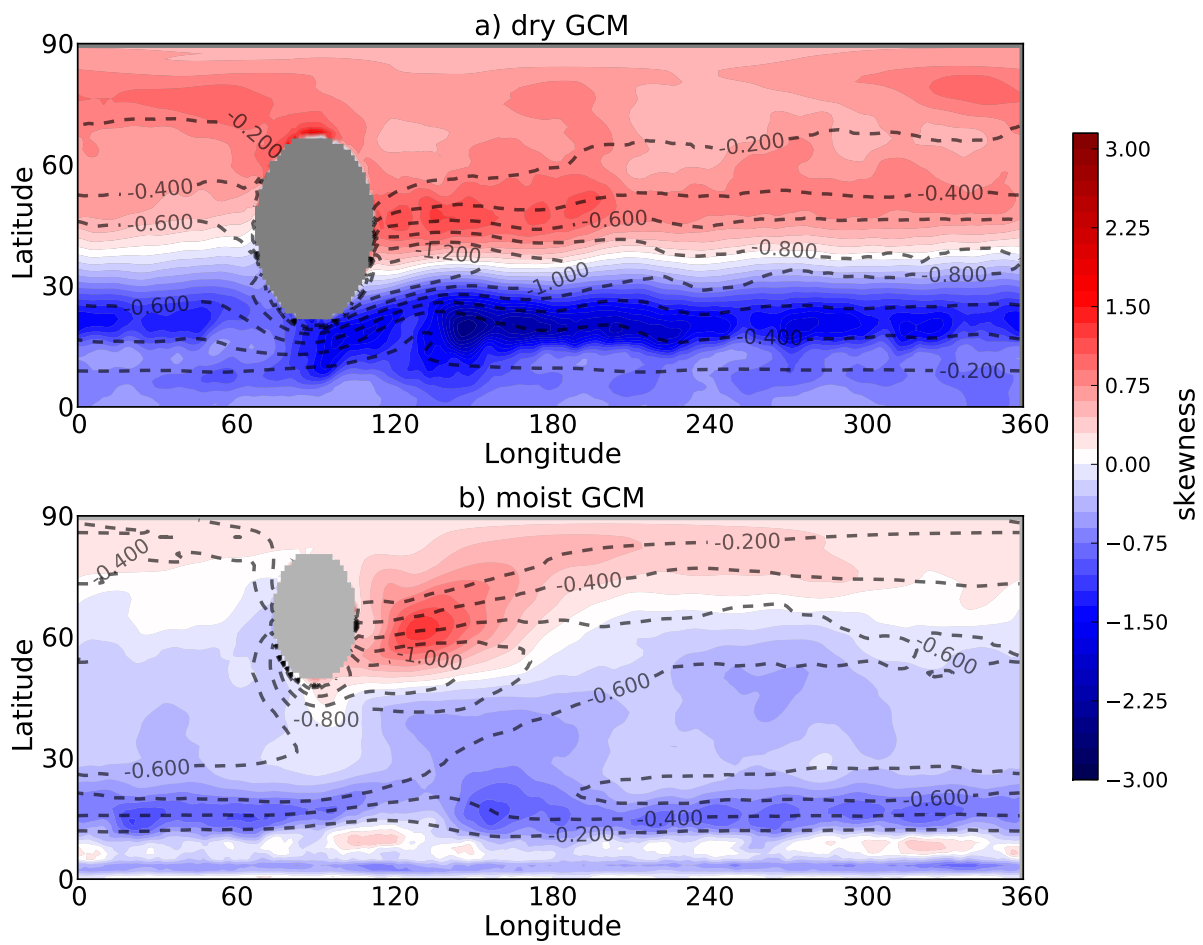
532 FIG. 8. a) Profiles taken at 35°N of synoptic-scale variance of DJF 850hPa potential temperature in the three
 533 simulations with FLOR. b) Profiles taken at 50°N. Gaps in the profiles show where topography intrudes into the
 534 850hPa level.



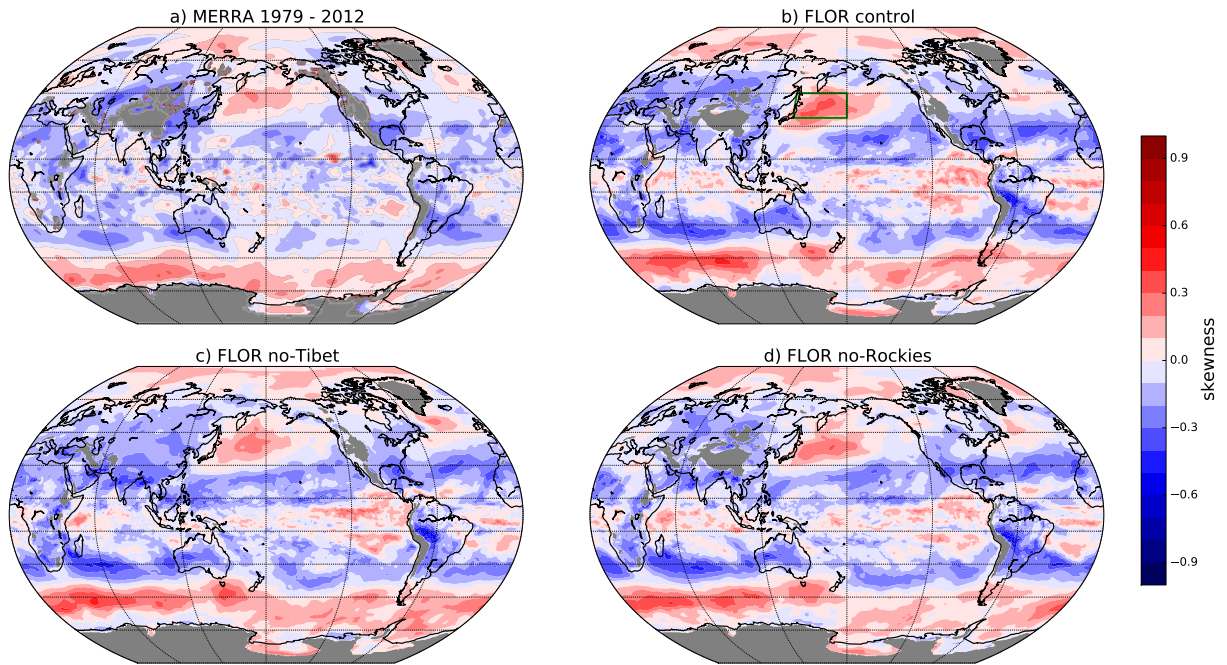
535 FIG. 9. a) DJF 850hPa temperature (contours) and total wind vectors in the vicinity of the Tibetan Plateau,
 536 averaged over the period 1979 to 2012. Data are taken from the MERRA re-analysis dataset. Locations where
 537 topography intrudes through 850hPa are masked in gray. b) Same for the region near the Rocky Mountains.



538 FIG. 10. Difference in DJF synoptic eddy kinetic energy (v^2) at 850hPa between the no-Tibet simulation and
539 the control simulation with FLOR



540 FIG. 11. a) Skewness of 850hPa synoptic temperatures (colored contours) and 850hPa meridional temperature
 541 gradients (black contours, contour interval = $0.2\text{K}(100\text{km})^{-1}$) in the dry GCM simulation with $H = 4\text{km}$. b)
 542 Same for the simulation with the moist GCM. The meridional gradient contour interval is $0.2\text{K}/100\text{km}$ in both
 543 panels.



544 FIG. 12. a) Skewness of DJF 850hPa synoptic temperatures for the period 1979-2012 in the MERRA data.
 545 b) Skewness of DJF 850hPa synoptic temperatures in the control simulation with FLOR. c) Skewness of DJF
 546 850hPa synoptic temperatures in the no-Tibet simulation with FLOR. d) Skewness of DJF 850hPa synoptic
 547 temperatures in the no-Rockies simulation with FLOR.